Unraveling the Origin of Unusual Shift in the Electroluminescence of 1D $CsCu_2I_3$ Light-Emitting Diodes

*Udara M. Kuruppu, Mohammad A. Rahman, and Mahesh K. Gangishetty**

Department of Chemistry, Mississippi State University, Mississippi State, MS, 39762, USA

Corresponding Author

Mahesh K. Gangishetty

E-mail: mgangishetty@chemistry.msstate.edu

ABSTRACT

Lead-free low-dimensional copper-based metal halides are promising luminescent materials for broadband LEDs owing to their broad self-trapped exciton (STE) emission. However, recently in 1D $CsCu_2I_3$, a discrepancy between their electroluminescence (EL) and photoluminescence (PL) has been observed. As a result, the overall output color from LEDs is significantly different than the anticipated emission. To unveil the origin of this discrepancy, here, we provide comprehensive analyses and show that the shift in the EL is neither caused by any structural/optical interactions between $CsCu_2I_3$ and electron transport layers (ETL) nor by the degradation of 1D $CsCu_2I_3$. Instead, it depends on the carrier imbalance on $CsCu_2I_3$, mainly due to the difference in electron mobility of the ETLs and the electron density on the $CsCu_2I_3$ layer. By varying the ETLs, different

colored 1D $CsCu_2I_3$ LEDs with peaks at 556 nm, 590 nm, and 620 nm are fabricated, and a maximum luminance of over 2000 Cd/m^2 is achieved for a 556 nm LED. Further, by limiting the electron mobility and injection to 1D $CsCu_2I_3$ using an insulating LiF layer at the $CsCu_2I_3$/ETL interface, more red-shifted LEDs are achieved confirming the critical role of electron density on the EL characteristics of 1D $CsCu_2I_3$.

INTRODUCTION

Recently, low-dimensional metal halides have generated significant research interest in many optoelectronic applications due to their remarkable photophysical properties. Among these, copper metal halides have emerged as a vital group due to their non-toxic nature and excellent optoelectronic properties, including simple synthesis and processing methods.[1,2] Cu(I)-based metal halides have been investigated in photodetectors,[3] X-ray scintillators,[4] image sensors,[5] temperature sensors,[6] memristors and neuromorphic computing,[7] fluorescent inks,[8] anti-counterfeiting and encryption applications.[9,10] Cu exhibits multiple coordination numbers, which can form 2D layers, 1D chains, and isolated 0D units.[11] Additionally, the Cu(I) metal halides have a wide range of structural tunability hence they can form several crystal phases, including $Cs_3Cu_2I_5$ (325-type), $CsCu_2I_3$(123-type), Cs_2CuI_3(213-type), Cs_2CuI_4(214-type), etc.[12–14] Each phase exhibits its own unique physical, chemical, and electronic properties that are distinct from others.

Among those, 1D $CsCu_2I_3$ has attracted attention due to efficient broadband yellow emission desirable for household and industrial lighting applications. However, attaining pure 1D $CsCu_2I_3$-phase in thin films for LEDs is one of the major challenges; often, thin film fabrication methods lead to unwanted phases that interfere with the optical and electronic properties. In addition, a discrepancy between their EL and PL spectra has been recently observed in most reports, where

the EL spectra do not perfectly overlap with the PL spectra. Some reports observed a shift in the EL peak, while others showed a broadening of the EL compared to the PL. In 2019, pioneering work by Roccanova and co-workers on $CsCu_2I_3$ LEDs observed an EL peak at 554 nm, which is 22 nm redshifted compared to the PL at 576 nm.[15] Shengnan and co-workers designed a white light-emitting diode (WLED) using a mixture of $Cs_3Cu_2I_5$ and $CsCu_2I_3$ and observed a broad EL at 571 nm that is redshifted compared to PL at 555 nm.[16] Similarly, Yunzhi and co-workers demonstrated $CsCu_2I_3$ LEDs with EL peak at ~ 600 nm, whereas the PL was at ~578 nm from ITO/PEDOT: PSS/$CsCu_2I_3$/TPBi/LiF/Al. They attributed this shift to a new radiative recombination center resulting from cuprous-iodide clusters formed by the migration of iodide ions under applied bias.[17] Recently, Rui Xu and co-workers fabricated yellow emitting LEDs using a composite emissive layer of $Cs_3Cu_2I_5$ and $CsCu_2I_3$ (ITO/m-PEDOT: PSS/$CsCu_2I_3$/TmPyPB/LiF/Al with a 565 nm peak EL wavelength. According to their observations, the EL shift is caused by the in-situ formation of a Cu(I) emissive center through the interaction of the copper iodide with the pyridine-based electron transport layers (ETLs) under applied bias.[18] In all these studies, although the same emissive layer (1D $CsCu_2I_3$) is used, each report observed a different EL peak depending on the device structure. Moreover, in each case, the EL and PL do not match, and the magnitude of the spectral shift between EL and PL is different. This unusual spectral mismatch can result in significant differences in the overall color output compared to estimated colors from their PL spectra. Note that color quality is one of the critical components in assessing the LEDs for commercial lighting applications. Any minor deviations from the desirable colors can prevent growth in the commercial market. Therefore, to rationally develop 1D $CsCu_2I_3$ LEDs for targeted lighting applications, the underlying reasons responsible for these unusual spectral deviations must be addressed.

Here, we systematically investigate the origin of spectral shift by employing phase-pure and bright yellow emitting 1D $CsCu_2I_3$ in LEDs. We constructed a series of 1D $CsCu_2I_3$ LEDs by rationally varying the ETLs and HTLs based on their mobilities and discovered that the shift is caused by the ETLs, not by the HTLs. By simply changing the ETL in a device, different colored LEDs with EL peaks at 556 nm (yellow), 590 nm (reddish yellow), and 647 nm (red) are demonstrated. In all these cases, there is a spectral mismatch caused by the broadening of the EL or by peak shift compared to their PL. With the help of steady-state and time-resolved PL, XRD, and ^{1}H NMR of pure $CsCu_2I_3$ and the mixture of $CsCu_2I_3$ and transport layers, we discovered that the origin of spectral mismatch is neither caused by a complex formation nor by the generation of any new radiative states nor by the degradation of 1D $CsCu_2I_3$. Instead, it is likely originated from the carrier imbalance caused by the presence of excess/insufficient electrons on the emissive layer. To test this hypothesis, we introduced a very thin insulating lithium fluoride (LiF) layer at the emissive layer/ETL interface and observed a further red shift in EL. Furthermore, a slight increase in the thickness of the LiF layer resulted in an even greater red shift in the EL peak position. These results show the influence of the electron mobility of the ETL and the electron density on the EL characteristics of the $CsCu_2I_3$.

RESULTS AND DISCUSSION

$CsCu_2I_3$ thin films are fabricated by spin-coating precursor salts from DMF and DMSO mixture and annealing at 80 °C. The detailed fabrication procedure is provided in the experimental section. Note that the stoichiometric ratio of precursors is very crucial for achieving phase pure cesium copper iodides. Otherwise, it can result in the formation of 0D $Cs_3Cu_2I_5$ and other phases that could interfere with 1D $CsCu_2I_3$ emission. To avoid these unwanted phases, the precursor ratio (CuI and CsI) must be precisely maintained at 2:1.[19] The purity of $CsCu_2I_3$ was verified by powder XRD,

shown in **Figure 1 (a)**. The diffraction pattern matches the standard 1D $CsCu_2I_3$ pattern (JCPDS #45-0076). The corresponding crystal structure is shown in **Figure 1 (b)**.

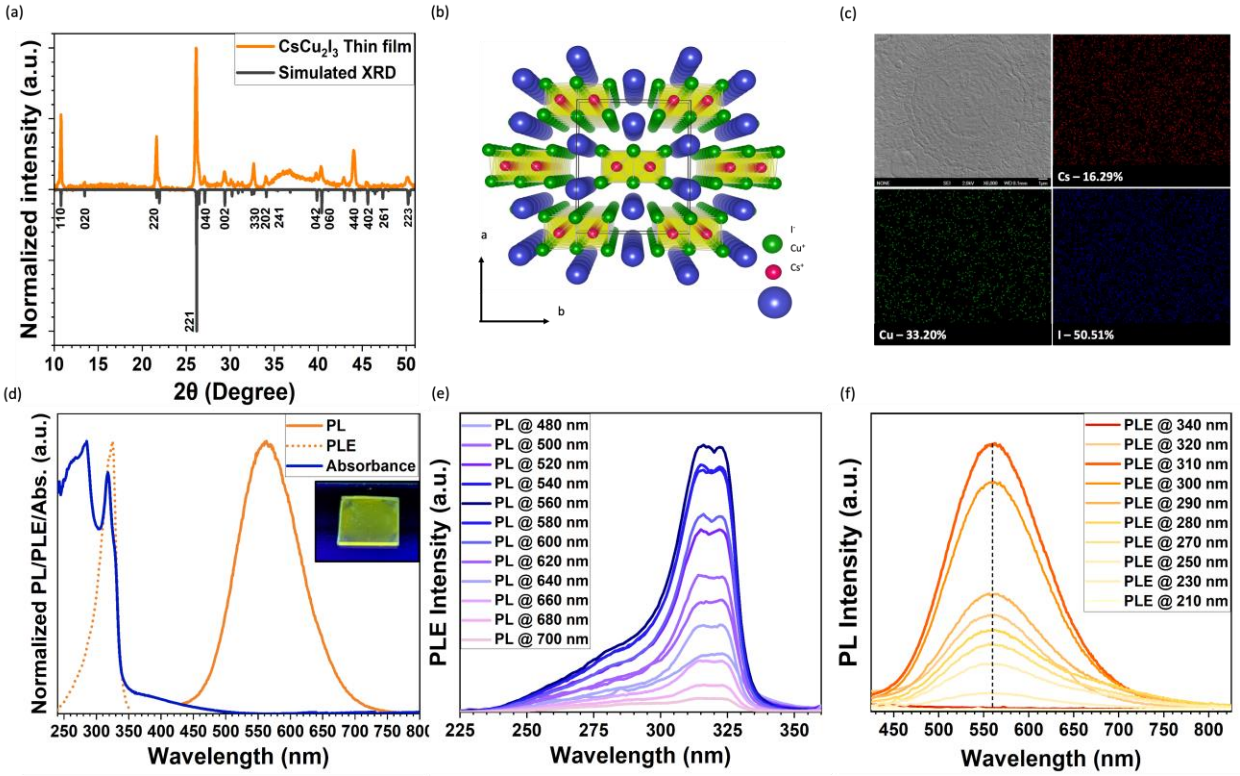

Figure 1. (a) P-XRD of $CsCu_2I_3$ and simulated pattern (b) Crystal structure of $CsCu_2I_3$ (c) SEM/EDAX analysis of $CsCu_2I_3$ thin film (d) UV-Vis absorption, photoluminescence excitation (PLE) and photoluminescence PL (The inset displays a photograph of $CsCu_2I_3$ thin film under 300 nm UV lamp) (e) Emission-wavelength dependent PLE spectra and (f) Excitation-wavelength dependent PL spectra

The $CsCu_2I_3$ adopts a base-centered monoclinic lattice (orthorhombic-C) structure with the **C*mcm*** space group.[20, 21] Further, SEM images along with their EDAX elemental mapping in **Figure 1c**

confirms the presence of Cs, Cu and I. Their compositional analyses in **Figure S1** reveal the ratio of Cs: Cu: I as 1:2:3 and further validate the formation of a pure 1D $CsCu_2I_3$ phase.

Next, their optical properties are investigated. Under 300 nm UV excitation, the thin films of $CsCu_2I_3$ showed bright yellow emission (inset of Fig1d). **Figure 1d** shows the absorption spectrum with an excitonic feature at 330 nm with a tail around 500 nm. The PL excitation (PLE) spectrum is recorded for the emission at 556 nm, which perfectly overlaps with the excitonic peak at 330 nm in the absorption spectrum, as shown in **Figure 1d**. The corresponding PL spectrum shows a broadband emission from 450 –700 nm with a full width at half-maximum (FWHM) of approximately 100 nm with a significant Stokes shift of around 230 nm. Such broad emission and large Stokes shift in metal halides is an indication that the emission originated from STEs by the excited state distortions, not originated by the band-edge states, as reported by many other groups.[22–24] In 1D $CsCu_2I_3$, the valence and conduction bands (VB and CB) primarily comprise Cu-3d and Cu-4s orbitals, respectively.[25] Upon illumination, the electron is promoted to the Cu-4s orbitals and facilitates the formation of one or more Cu-Cu bonds with the neighborhood Cu atoms[25,26] through the hybridization of the Cu- 4s orbital. Within the proximity, several Cu atoms (**Figure 1 b**) in the neighborhood increase the chances of the Cu−Cu bond formation upon excitation. This Cu-Cu bond exerts strain on the Cu-I bonds and distorts the lattice.[27–29] Overall, the process of STE involves a significant structural distortion, which includes the breaking and forming of multiple bonds upon the excitation.[25] These lattice distortions are responsible for forming new radiative states, often called STE states, and result in broad emission.[25] Further, to confirm the emission originated from STE, we recorded the PLE spectra by varying the emission wavelengths. As shown in Figure 1e, regardless of the emission wavelength, the same PLE spectral pattern was observed, except for a decrease in intensity. Similarly, emission spectra are recorded

under various excitations and observed no change (Fig 1f). No changes in the emission/excitation peaks further confirm the absence of other unwanted phases in the thin films.[28]

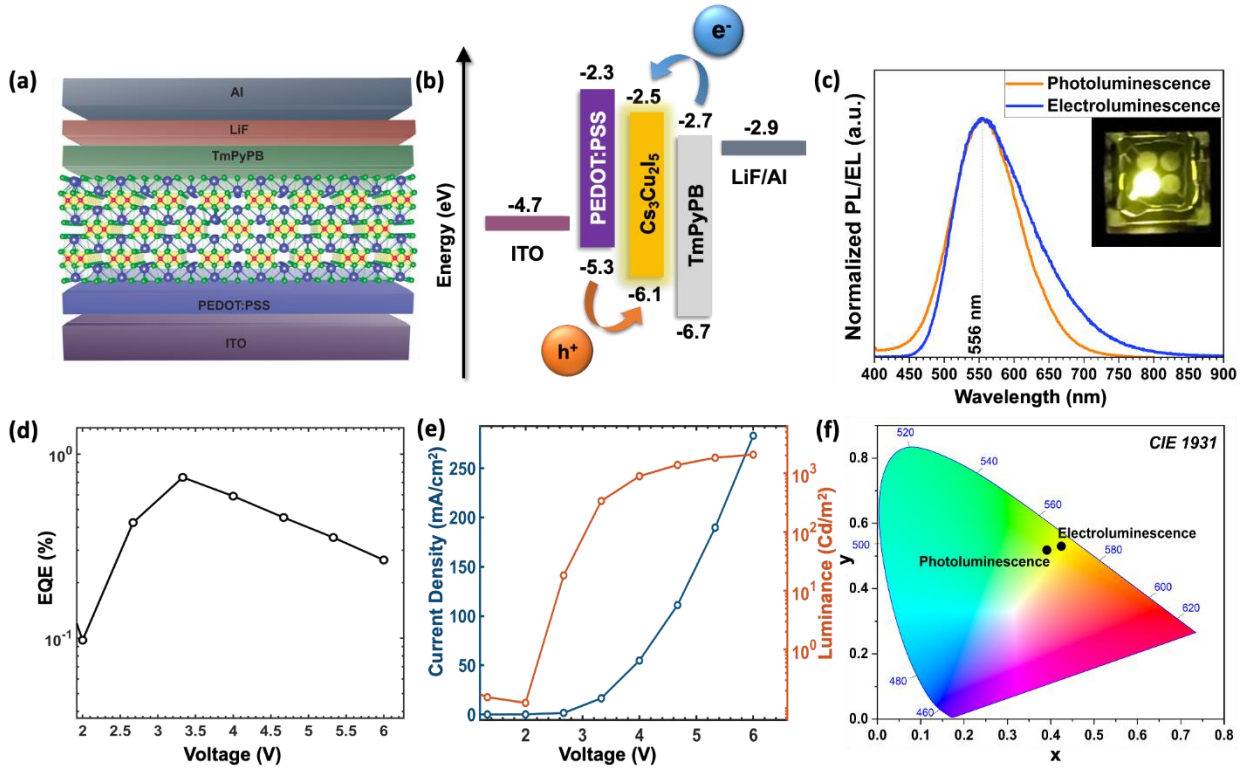

Figure 2. (a) Schematic illustration of the LED heterostructure of ITO/PEDOT:PSS/$CsCu_2I_3$/TmPyPB/LiF/Al (b) Overall energy band diagram of the LED structure (c) The EL spectra of the LED and the PL spectra of the $CsCu_2I_3$ (The inset shows a photograph of the working LED) (d) EQE as a function of voltage for the LED (e) Current density and luminance as a function of voltage for the LED (f) CIE color coordinates of the EL and PL of $CsCu_2I_3$

Next, we constructed light-emitting diodes (LEDs) using these 1D $CsCu_2I_3$ using a device architecture ITO/PEDOT:PSS/$CsCu_2I_3$/TmPyPB/LiF/Al (shown in **Figure 2a**). The detailed fabrication procedure is provided in the experimental section. The corresponding energy level diagram of all the layers is shown in **Figure 2b**; the values are obtained from the literature.[30,31] The LEDs resulted in broad and bright yellow emission with an EL peak at 556 nm (**Figure 2c** inset shows the image of LED). The current density-voltage-luminance (J-V-L) characteristics and the external quantum efficiency (EQE) are recorded and plotted against voltage. From the *JVL* plot (**Figure 2e**), the device exhibits a turn-on voltage of 3.0 V with a maximum luminance over 2000 Cdm^{-2}. Corresponding EQE data is plotted in **Figure 2d**, which shows the peak value of 0.75%. As shown in **Figure 2c**, although both EL and PL have an emission peak at 556 nm, they do not perfectly overlap. The EL is broader than the PL and has a red tail that is absent in the PL. This deviation resulted in a clear distinction in their output color, as depicted in the CIE 1931 (Commission Internationale de l'Eclairage) chromaticity diagram in **Figure 2(f)**. This diagram is often used as a reliable platform to assess whether the output color from LEDs meets the requirements of the commercial market or not.[32] From the chromaticity diagram, the color coordinates for the PL are (0.392, 0.518) and the EL are (0.424, 0.529). Interestingly, similar discrepancies in EL and PL have been observed by various studies in the literature. In many cases, a shift in the EL peak is observed compared to the PL; all the results from previous reports are summarized in **Table S2**. [15–17,33]

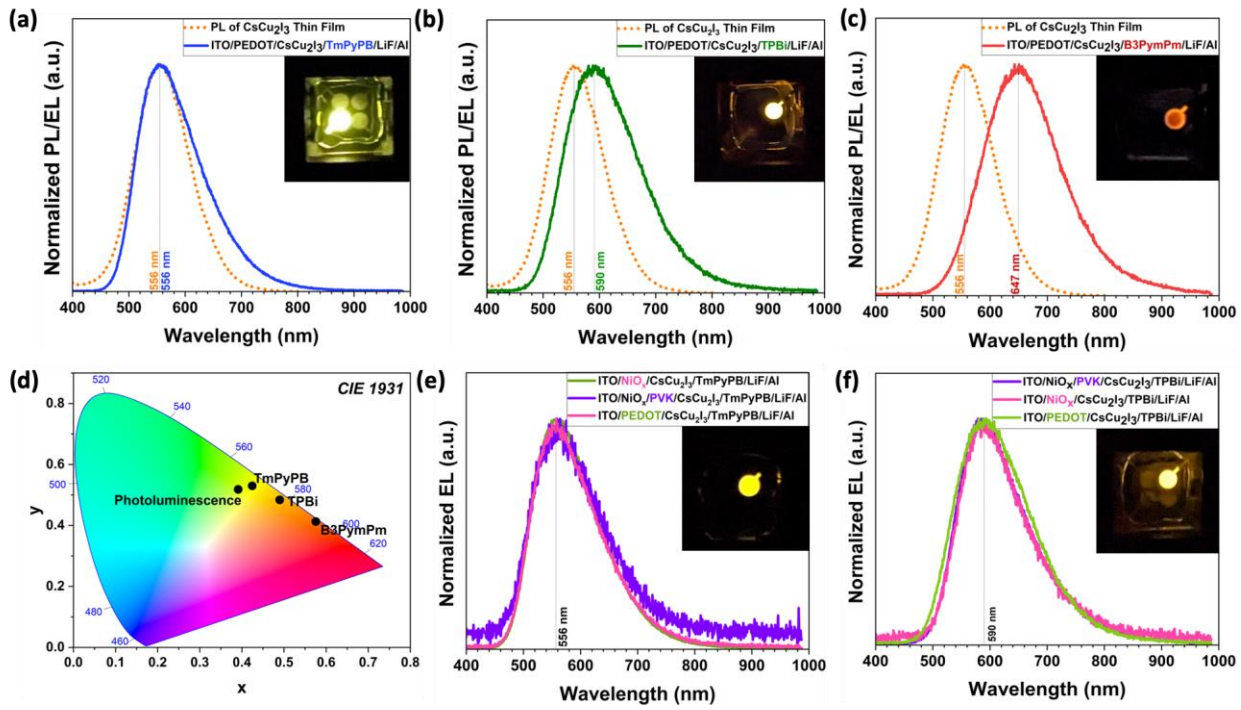

Figure 3. (a) The PL spectra of the $CsCu_2I_3$ and the EL spectra of ITO/PEDOT:PSS/$CsCu_2I_3$/**TmPyPB**/LiF/Al LED (inset displays the working LED) (b) ITO/PEDOT:PSS/$CsCu_2I_3$/**TPBi**/LiF/Al LED (inset displays the working LED) (c) ITO/PEDOT:PSS/ $CsCu_2I_3$/**B3PymPm**/LiF/Al LED (inset displays the working LED) (d) CIE color coordinates of the PL of $CsCu_2I_3$ and EL of the LEDs of different ETLs (e) The PL spectra of the $CsCu_2I_3$ and the EL spectra of ITO/**NiO_x**/$CsCu_2I_3$/TmPyPB/LiF/Al LED (inset displays the working LED) and ITO/NiO_x/**PVK**/$CsCu_2I_3$/TmPyPB/ LiF/Al LED (f) ITO/NiO_x/$CsCu_2I_3$/TPBi/LiF/Al LED (inset displays the working LED) and ITO/NiO_x/**PVK**/$CsCu_2I_3$/ TPBi/LiF/Al LED

To get more insights into the discrepancy between the EL and PL, we constructed a series of devices by varying ETLs and HTL while using 1D $CsCu_2I_3$ as the emissive layer. First, we varied ETLs using TPBi, B3PymPm, and TmPyPB while keeping the rest of the device structure the same. The EL spectrum of each device is recorded and compared with the PL. As shown in **Figure**

3 (a-c), the EL spectra are substantially different in each case. By simply varying the ETL, we were able to achieve bright yellow, reddish-yellow, and red-emitting LEDs with peaks at 556 nm, 590 nm, and 647 nm, respectively, for TmPyPB, TPBi, and B3PymPm. While the EL peak of TmPyPB matches with the PL, the TpBi and B3PymPm showed ~34 nm and 91 nm redshift compared to the PL. When the EL spectra were transformed to the CIE 1931 color space (**Figure 3d**), we observed a striking difference in the color coordinates (**Table S1**). Further, to study if HTLs have any role in the STE emission, we varied HTLs such as PEDOT: PSS, PVK, and NiO_x and kept the ETLs the same. We studied this for two ETLs, TmPyPB and TPBi. In both cases, despite a change in the HTLs from PEDOT:PSS to PVK or NiO_x, the EL peak remained almost the same (**Figure 3e-f**). Unfortunately, ITO/NiO_x/$CsCu_2I_3$/B3PymPm/LiF/Al LED did not light up, obstructed from studying the effect of change in HTL in B3PymPm devices. The EL spectra of all these devices are plotted on the CIE 1931 diagram (**Figure S4**) and observed almost negligible changes in the color coordinates (**Table S1**). Based on these device analyses, it is evident that the ETL is playing a major role in the shift in EL compared to PL. Note that these ETLs are rationally selected based on their electron mobilities (TmPyPB > TpBi > B3PymPm). Therefore, due to the difference in their electron mobilities, the net electron density on the emissive layer is different, which perhaps is a critical factor in altering structural distortions and, hence, the emission from STEs. However, in addition to this, there could be several other possible reasons responsible for the shift in EL, which include 1) structural interactions between ETL and Cu under applied bias resulting in the formation of a new emissive species that could be either Cu complex or different phase of copper halides, 2) formation of new radiative states from the excited state interactions of 1D $CsCu_2I_3$ and ETLs, and 3) degradation/oxidation-reduction of 1D $CsCu_2I_3$ under applied bias.

The role of each of these effects is systematically investigated to determine the underlying reason for the shift. To verify if there is any change in crystal structure or phase change of the $CsCu_2I_3$ in the presence of ETLs, we recorded the powder XRD of $CsCu_2I_3$ by mixing with ETLs. The thin films were fabricated by spin-coating the mixture of the ETL and $CsCu_2I_3$ precursor solution. As shown in **Figure 4a**, the diffraction patterns of the $CsCu_2I_3$ when mixed with the ETL are identical to the pristine $CsCu_2I_3$ and perfectly overlap with pure 1D phases of $CsCu_2I_3$, indicating that there is no change in the crystal structure. Simultaneously, we recorded the ^1H NMR of each ETL (TmPyPB, TPBi, and B3PyMPM) in the presence of $CsCu_2I_3$, CsI, and CuI to determine if there is any complex formation/interaction between Cu^+, Cs^+ and ETL. It has been reported that the Cu^+ in the copper halides can form a complex with ETLs with the chelating nitrogen on pyridine or pyrrole rings on the ETL.[18] These pyridine or pyrrole groups act as Lewis bases and are capable of donating a lone pair of electrons to the vacant d-orbitals of Cu^+ to form a coordinate covalent bond. [34] Such complex formation with 1D $CsCu_2I_3$ can be easily studied by ^1H NMR. The ^1H NMR spectra of each ETL were collected with and without the mixing of $CsCu_2I_3$, CuI, and CsI. For TPBi and B3PymPm, $CDCl_3$ was used, and for TmPyPB, we chose Toluene-d_8 due to the poor solubility of TmPyPB in $CDCl_3$. **Figure 4 (b, c, and d)** shows the comparison of ^1H NMR spectra of pure ETLs (TmPyPB, TPBi, and B3PymPm) and ETLs mixed with $CsCu_2I_3$, CuI, and CsI. The inset of Fig 4b, c, and d show the selected regions in the ^1H NMR spectra that correspond to the deshielded region of protons neighborhood to the N groups of pyridine or pyrrole rings. The full spectra of all the samples are shown in **Figure S5-7**. These neighborhood protons are expected to be more affected by the chelation/interaction of N with the Cu of $CsCu_2I_3$. The resonances corresponding to these protons are at δ 8.69 and δ 8.24 ppm for TmPyPB, δ 7.76 and δ 7.36 ppm for TpBi, and δ 8.93 and δ 8.62 ppm for B3PymPm.

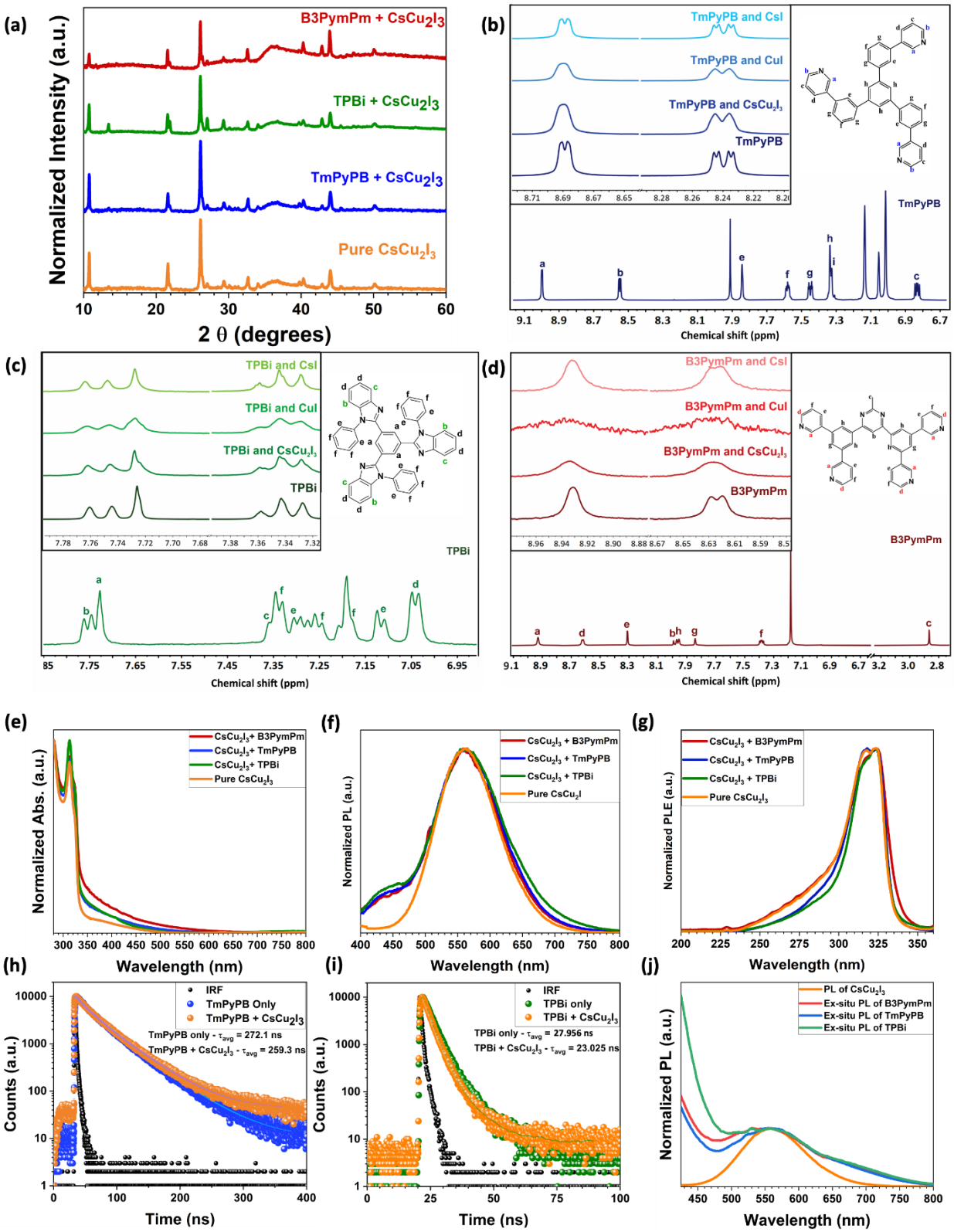

Figure 4. (a) P-XRD of pure $CsCu_2I_3$ and ETL mixed $CsCu_2I_3$ (b) ^1H NMR of TmPyPB (c) ^1H

https://doi.org/10.26434/chemrxiv-2023-v0c16-v2 **ORCID:** https://orcid.org/0000-0002-1680-1457

NMR of TPBi (d) ^{1}H NMR of B3PymPm (e) UV-Vis absorbance of pure $CsCu_2I_3$ and ETL mixed $CsCu_2I_3$ (f) PL spectra of pure $CsCu_2I_3$ and ETL mixed $CsCu_2I_3$ (g) PLE spectra of pure $CsCu_2I_3$ and ETL mixed $CsCu_2I_3$ (h) TRPL of TmPyPB (i) TRPL of TPBi (j) PL of the devices after operated (λ_{EX} = 300 nm)

In all three cases, no significant chemical shift was observed when mixed with $CsCu_2I_3$, CsI, and CuI. However, there was a moderate to extreme broadening/suppression of the signal depending on the sample mixture. Interestingly, the peak broadening in TmPyPB is more prominent when mixed with CuI and $CsCu_2I_3$ (**Figure 4b**) compared to others, although the TmPyPB device showed a negligible peak shift in the EL. On the contrary, the TPBi samples showed no peak broadening/suppression when mixed with $CsCu_2I_3$, CsI, and CuI despite the striking red shift in the EL (**Figure 4c**). In the case of B3PymPm, we observed significant peak broadening in all cases (**Figure 4d**); the B3PymPm signals are suppressed when mixing with CuI. Note that the Cu^{+} in this mixture can be easily oxidized to paramagnetic $Cu^{2+}$and it can create local magnetic fields that are different from the applied magnetic field, which may lead to significant line broadening or signal suppression.[35,36] Overall, the changes in ETL resonances in the presence of $CsCu_2I_3$ are insignificant; therefore, there is no concrete evidence supporting the complex formation between $CsCu_2I_3$ and ETLs from NMR data.

Next, we investigate the changes in optical properties of $CsCu_2I_3$ by mixing with ETLs to understand if there is any energy exchange or reabsorption causing the spectral mismatch. Here, we mixed ETL with the $CsCu_2I_3$ precursor solution to prepare the thin films for optical analyses. As shown in **Figure 4e**, the band-edge absorption remained the same for (ETLs+ $CsCu_2I_3$) thin films as the pristine $CsCu_2I_3$ layers. In addition, no changes in PL and PLE spectra of $CsCu_2I_3$ were observed with the mixing of ETLs (**Figure 4 f and g**). Next, the excited state decay profiles

of ETLs (TmPyPB at 340 nm and TPBi at 390 nm) were recorded by mixing them with $CsCu_2I_3$. As depicted in **Figures 4 h and i**, the changes were modest for both TPBi and TmPyPB in the presence of $CsCu_2I_3$. The TmPyPB showed some deviation in the longer timescales, and the TPBi showed faster decay in the earlier times. Since there is no shift in the PL peak position after mixing with ETLs, along with no major changes in the TRPL data, the possibility of the formation of new recombination centers can be ruled out. Further, to study the degradation of $CsCu_2I_3$ (typically due to iodide migration) under applied bias on the spectral shift, we recorded the PL spectra before and after operating the LED at 5 mA for 2 minutes. As shown in **Figure 4 j**, the PL peak remained unchanged before and after stressing the device, indicating that there was no change in the composition of $CsCu_2I_3$. Therefore, the possibility of degradation-induced spectral shift can also be excluded.

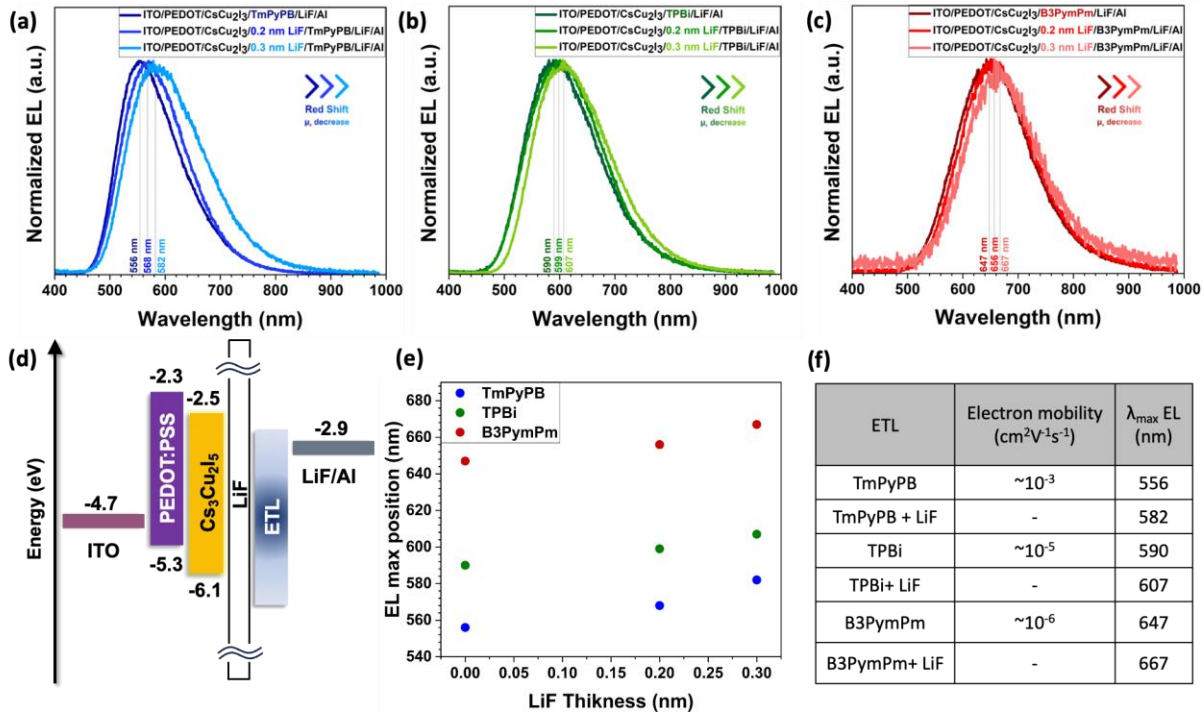

ETL	Electron mobility ($cm^2V^{-1}s^{-1}$)	λ_{max} EL (nm)
TmPyPB	~10^{-3}	556
TmPyPB + LiF	-	582
TPBi	~10^{-5}	590
TPBi+ LiF	-	607
B3PymPm	~10^{-6}	647
B3PymPm+ LiF	-	667

Figure 5. (a) The EL spectra of ITO/PEDOT:PSS/$CsCu_2I_3$/TmPyPB/LiF/Al with introducing LiF insulating layer (b) ITO/PEDOT:PSS/$CsCu_2I_3$/TPBi/LiF/Al with introducing LiF (0.2 nm and 0.3

nm) insulating layer (c) ITO/PEDOT:PSS/$CsCu_2I_3$/B3PymPm/LiF/Al with introducing LiF (0.2 nm and 0.3 nm) insulating layer (d) Schematic illustration of the LED heterostructure of ITO/PEDOT:PSS/$CsCu_2I_3$/LiF/ETL/LiF/Al (e) EL peak position versus the thickness of LiF layer (f) electron mobility of ETLs and peak electroluminescence wavelength.

From all these analyses, it is most likely that the carrier imbalance on the emissive layer is causing the shift in EL. The imbalance in electron and hole injection can cause an uneven distribution of charge carriers in the crystal lattice of $CsCu_2I_3$.[37] Note that the emission in these copper halides originates from excited structural distortions (STEs); therefore, the difference in electron/hole density in the VB and CB of $CsCu_2I_3$ can alter the distortions and affect the emission from STEs. In addition, the accumulation of excess charge in specific regions outside the charge-neutral/radiative recombination zones within $CsCu_2I_3$ and at the HTL/$CsCu_2I_3$ and $CsCu_2I_3$/ETL interface can influence the characteristics of EL emission.[38] In the present case, the redshift shift is observed only when the ETL is changed, and the mobilities of the ETL, TmPyPB, TPBi, and B3PymPm used here are on the order of $\sim 10^{-3}$, $\sim 10^{5}$, and $\sim 10^{-6}$ $cm^2\ V^{-1}\ s^{-1}$ respectively.[39–41] With the decrease in the electron mobility of the ETL, the magnitude of the red shift in the EL increases, which implies that the difference in electron density on the emissive layer plays a critical role in the shift in EL. In an LED, the electrons are directly injected into the CB of the $CsCu_2I_3$, and the CB is composed of 4s orbital. As discussed earlier, promoting electrons into these 4s orbitals leads to structural distortions and broad emission from STEs. Each ETL, depending on the electron mobility, injects a different number of electrons into the CB of $CsCu_2I_3$ and, therefore, can induce different magnitudes of structural distortions and different emission peaks in EL. To test our hypothesis that the difference in electron density is responsible for the emission shift, we introduced a very thin insulating layer of lithium fluoride (LiF) between the emissive layer and the

ETL in a device, and their EL spectra are recorded (**Figure 5 a-c**). The LiF layer, being characterized by a relatively high electron affinity and wide band gap (**Figure 5d**), creates an energy barrier and impedes the movement of electrons from the ETL into $CsCu_2I_3$.[42,43] Interestingly, with the introduction of a 0.2 nm thin insulating layer, the EL emission is red-shifted when compared to the control device. A device with TmPyPB as ETL showed an EL peak at 556 nm, which is redshifted to 564 nm after introducing 0.2 nm LiF layer. With an increase in the thickness of the LiF layer to 0.3 nm, we observed a further red shift of the EL emission to 586 nm. The same trend is observed in devices containing TPBi and B3PymPm as ETLs (**Figure 5b and c**). These results confirm that the shift in the EL peak compared to PL is due to a change in electron density on the $CsCu_2I_3$ with a change in the ETL. While there are several reports demonstrating the STE emission is triggered by the photo-excited, our results highlight the fact that the STEs in copper halides are triggered and controlled by the electrically pumped free carriers in $CsCu_2I_3$.

CONCLUSION

This study has successfully provided a comprehensive understanding of the underlying factors driving the EL and PL peak shift observed in 1-D $CsCu_2I_3$. Our ^{1}H NMR, steady-state, and time-resolved PL studies revealed that this discrepancy in peak wavelengths is not attributed to inherent interactions (neither structural nor optical) between Cu and ETL but rather influenced by the electron mobility of ETL. Furthermore, by introducing a LiF insulating layer at the $CsCu_2I_3$/ETL interface, we demonstrated the STE emission can be effectively controlled by changing the electron mobility in the device. With an increase in the thickness of the insulating layer, a systematic increase in the red shift in peak EL emission accentuates the direct relationship between the electron mobility of the ETL and the EL characteristics of $CsCu_2I_3$.

METHODOLOGY

Materials

Cesium iodide (CsI, 99.999%), Copper iodide (CuI, 98%), DMF (N, N-Dimethylformamide-anhydrous, 99.8%), DMSO (Dimethyl sulfoxide-anhydrous, ≥99.9%), Toluene D8 (Toluene-d8, 99.6 atom % D), Chloroform-d (99.8 atom % D), Acetone (ACS reagent, ≥99.5%), Isopropyl alcohol - 2-Propanol (HPLC, 99.9%), Ethylene glycol (Reagent Plus, ≥99.5%), Zinc acetate dihydrate (99.999%), Nickel(II) nitrate hexahydrate (99.999%), and Lithium fluoride (LiF, ≥99.98%) were purchased from Sigma Aldrich. Poly (styrene sulfonate) (PEDOT: PSS) was purchased from Heraeus Epurio. 2,2',2''-(1,3,5-benzinetriyl)-tris(1-phenyl-1-H-benzimidazole) (TPBi, >99.8%), 1,3,5-Tri(m-pyridine-3 -ylphenyl) benzene (TmPyPB, >99.8%), 4,6-Bis(3,5-di(pyridine-3-yl)phenyl)-2-methylpyrimidine, 4,6-Bis(3,5-di-3-pyridinylphenyl)-2-methylpyrimidine (B3PymPm, >99%) were purchased from Luminescence Technology Corp. No additional purification was performed on the materials before use.

Preparation of the cesium copper iodide precursor solution

The cesium copper iodide precursor solution was prepared by dissolving 259.81 mg (1 mmol) of CsI and 380.9 mg (2 mmol) of CuI in 2 mL of DMF and DMSO mixture (DMF: DMSO = 1:1 in volume). The precursor solution was stirred for 1 hour in the glove box (oxygen and moisture levels below 0.1 ppm) at 60 ℃. Then, the precursor solution was filtered with a 0.22 PTFE filter to obtain the transparent yellow color solution.

Preparation of the NiO_x precursor solution

The NiO_x precursor solution was prepared by using a procedure based on a previous report.[44] To prepare the NiO_x precursor solution, 1.5 mL of $Ni(NO_3)_2.6H_20$ and Ethelene diammine were dissolved in ethylene glycol, resulting in the formation of a blue-colored complex. The solution was stirred for 10 minutes at room temperature and filtered using a 0.4 mm PVDF filter.

Preparation of samples for NMR Analysis

For the preparation of TmPyPB sample series, approximately 5 mg of TmPyPB and 1 mg of $CsCu_2I_3$ were dissolved in Toluene d-8. Approximately 5 mg of TmPyPB and 1 mg of CuI /1 mg of CsI salt were dissolved in Toluene d-8. For the preparation of the TPBi and B3PymPm sample series, approximately 5 mg of TPBi and 1 mg of $CsCu_2I_3$/1 mg of CuI /1 mg of CSI salt were dissolved in $CDCl_3$.

Device Fabrication

The patterned Indium tin oxide (ITO) glass substrates (12.2 x 12.2 mm^2, 15 Ω) were washed by sonication using Decon 90 detergent, followed by a sequential wash for 10 minutes using deionized water (two times), and acetone. Then, the ITO substrates were cleaned in boiling 2-IPA for 10 minutes and dried with airflow. The substrates were further cleaned with UV-Ozone plasma cleaner (PIE Scientific Tergeo Plus) for a duration of 7 minutes at a power of 20 W. The filtered (0.45 μm PTFE) PEDOT: PSS (40 μL) solution was employed as the hole transport layer (HTL) and spin-coated onto the ITO substrate at 4000 r.p.m for 45 s. Then the substrates were transferred to a nitrogen-filled Glovebox and annealed for 15 min at 140 °C in order to eliminate any residual water. Precisely, 40 μl of cesium copper iodide precursor solution was dropped onto the substrate and spun by using two steps of the spin-coating program at 500 rpm for 5 s and then at 6000 rpm for 40 s. Later, the substrates were placed on a hot plate and annealed at 80 °C for 10 minutes to

obtain the $CsCu_2I_3$ active layer. Finally, the electron transport layer (TmPyPB, 50 nm), LiF (1 nm), and cathode (Al, 80 nm) were deposited sequentially onto the perovskite layer via thermal evaporation under a high vacuum of 5×10^{-6} mbar. Finally, the devices were encapsulated with a glass coverslip with epoxy resin inside the glovebox. All the other electron transfer layers (TPBi or B3PyPMP) were used in place of TmPyPB in the abovementioned device structure. Also, the NiO_x was used as a hole transport layer in place of PEDOT: PSS for some of the devices. The active area of the device is 3.14 mm^2 (2 mm in diameter) as defined by the overlapping area of the ITO and Al electrodes.

Material characterization

Powder XRD is recorded using PROTO, AXRD benchtop powder diffraction system equipped with Cu Kα (1.54 Å) radiation. Diffuse reflectance spectra are recorded using a Shimadzu UV-2600i UV–visible spectrophotometer. NMR experiments were performed using Bruker AVANCE III ($\nu_0(^1H)$ = 500 MHz) NMR spectrometer. The analysis of the diffuse reflectance spectra is performed using the Kubelka–Munk transformation. For measuring the steady-state photoluminescence (PL) and PL excitation (PLE) spectra, an Edinburgh FS5 spectrofluorometer is employed. Time-resolved photoluminescence (TRPL) measurements are conducted using the Deltaflex modular TCSPC lifetime system, Horiba Scientific, which is equipped with a 356 nm LED source.

Device characterization

We followed deMello's method for measuring *JVL* curves and EQEs.[45] Prior to measurement, all devices underwent packaging. Electroluminescence spectra were captured using an Ocean Optics QE Pro, with a device sourcing of 1 mA from a Keithley 2604B. J-V-L curves were obtained using

a calibrated Thorlabs photodiode that was physically positioned just above the device's surface. The device itself, with a radius of 1 mm, is considerably smaller than the detector. The overall device measurement configuration is combined with a 3D printed device holder (black material), effectively preventing the collection of waveguided light and avoiding overestimation of the External Quantum Efficiency (EQE).

Author Information: Corresponding Author, Notes

Author Contribution: U.M.K. synthesized the materials and fabricated all LEDs. U.M.K and M.K.G. performed all characterizations of the material and the devices. A. M. provided helpful discussions on electron mobility. M.K.G. supervised and guided the project, the first draft was written by U.M.K. and all the authors contributed equally to editing and revising the manuscript.

Acknowledgment: We would like to thank Nirosh Udayanga for his assistance with NMR data analysis, Bruno Donnadieu for running the samples on P-XRD, Dr. Rooban Venkatesh for SEM/EDAX imaging, and Dr. Anuraj Kshirsagar for his support on XRD data fitting. We thank Pro. Santnu Kundu for allowing the access to PL and PLE measurement setup.

Funding: (1) NSF Track 1 EPSCoR funding grant no. 1757220.

REFERENCES

(1) Cortecchia, D.; Dewi, H. A.; Yin, J.; Bruno, A.; Chen, S.; Baikie, T.; Boix, P. P.; Grätzel, M.; Mhaisalkar, S.; Soci, C.; Mathews, N. Lead-Free MA2CuClxBr4-x Hybrid Perovskites. *Inorg Chem* **2016**, *55* (3), 1044–1052. https://doi.org/10.1021/ACS.INORGCHEM.5B01896/ASSET/IMAGES/IC-2015-018962_M004.GIF.

(2) Jun, T.; Sim, K.; Iimura, S.; Sasase, M.; Kamioka, H.; Kim, J.; Hosono, H. Lead-Free Highly Efficient Blue-Emitting Cs3 Cu2 I5 with 0D Electronic Structure. *Adv Mater* **2018**, *30* (43). https://doi.org/10.1002/ADMA.201804547.

(3) Zhang, Z. X.; Li, C.; Lu, Y.; Tong, X. W.; Liang, F. X.; Zhao, X. Y.; Wu, D.; Xie, C.; Luo, L. B. Sensitive Deep Ultraviolet Photodetector and Image Sensor Composed of Inorganic Lead-Free Cs3Cu2I5 Perovskite with Wide Bandgap. *Journal of Physical Chemistry Letters* **2019**, *10* (18), 5343–5350. https://doi.org/10.1021/ACS.JPCLETT.9B02390/ASSET/IMAGES/LARGE/JZ9B02390_0006.JPEG.

(4) Zhao, X.; Niu, G.; Zhu, J.; Yang, B.; Yuan, J. H.; Li, S.; Gao, W.; Hu, Q.; Yin, L.; Xue, K. H.; Lifshitz, E.; Miao, X.; Tang, J. All-Inorganic Copper Halide as a Stable and Self-Absorption-Free X-Ray Scintillator. *Journal of Physical Chemistry Letters* **2020**, *11* (5), 1873–1880. https://doi.org/10.1021/ACS.JPCLETT.0C00161/SUPPL_FILE/JZ0C00161_SI_001.PDF.

(5) Zhang, Z. X.; Li, C.; Lu, Y.; Tong, X. W.; Liang, F. X.; Zhao, X. Y.; Wu, D.; Xie, C.; Luo, L. B. Sensitive Deep Ultraviolet Photodetector and Image Sensor Composed of Inorganic Lead-Free Cs3Cu2I5 Perovskite with Wide Bandgap. *J Phys Chem Lett* **2019**, *10* (18), 5343–5350. https://doi.org/10.1021/ACS.JPCLETT.9B02390.

(6) Zhang, Y.; He, Y.; Tang, Z.; Yu, W.; Zhang, Z.; Chen, Z.; Xiao, L.; Shi, J. jie; Wang, S.; Qu, B. Spontaneous Formation of Lead-Free Cs3Cu2I5 Quantum Dots in Metal–Organic-Frameworks with Deep-Blue Emission. *Small* **2022**, *18* (22), 2107161. https://doi.org/10.1002/SMLL.202107161.

(7) Zeng, F.; Guo, Y.; Hu, W.; Tan, Y.; Zhang, X.; Feng, J.; Tang, X. Opportunity of the Lead-Free All-Inorganic Cs3Cu2I5 Perovskite Film for Memristor and Neuromorphic Computing Applications. *ACS Appl Mater Interfaces* **2020**, *12* (20), 23094–23101. https://doi.org/10.1021/ACSAMI.0C03106/SUPPL_FILE/AM0C03106_SI_001.PDF.

(8) Zhang, F.; Zhao, Z.; Chen, B.; Zheng, H.; Huang, L.; Liu, Y.; Wang, Y.; Rogach, A. L. Strongly Emissive Lead-Free 0D Cs3Cu2I5 Perovskites Synthesized by a Room Temperature Solvent Evaporation Crystallization for Down-Conversion Light-Emitting Devices and Fluorescent Inks. *Adv Opt Mater* **2020**, *8* (8), 1901723. https://doi.org/10.1002/ADOM.201901723.

(9) Zhang, X.; Zhou, B.; Chen, X.; Yu, W. W. Reversible Transformation between Cs3Cu2I5and CsCu2I3Perovskite Derivatives and Its Anticounterfeiting Application. *Inorg Chem* **2022**, *61* (1), 399–405. https://doi.org/10.1021/ACS.INORGCHEM.1C03021/ASSET/IMAGES/LARGE/IC1C03021_0006.JPEG.

(10) Zhang, F.; Liang, W.; Wang, L.; Ma, Z.; Ji, X.; Wang, M.; Wang, Y.; Chen, X.; Wu, D.; Li, X.; Zhang, Y.; Shan, C.; Shi, Z. Moisture-Induced Reversible Phase Conversion of Cesium Copper Iodine Nanocrystals Enables Advanced Anti-Counterfeiting. *Adv Funct Mater* **2021**, *31* (47), 2105771. https://doi.org/10.1002/ADFM.202105771.

(11) Hull, S.; Berastegui, P. Crystal Structures and Ionic Conductivities of Ternary Derivatives of the Silver and Copper Monohalides—II: Ordered Phases within the (AgX)x–(MX)1−x and (CuX)x–(MX)1−x (M=K, Rb and Cs; X=Cl, Br and I) Systems. *J Solid State Chem* **2004**, *177* (9), 3156–3173. https://doi.org/10.1016/J.JSSC.2004.05.004.

(12) Sun, Z.; Chen, X.; Yin, W. Comprehensive First-Principles Studies on Phase Stability of Copper-Based Halide Perovskite Derivatives A l Cu m X n (A = Rb and Cs; X = Cl, Br, and I). *J. Semicond 2020* (5), 52201. https://doi.org/10.1088/1674.

(13) Yao, J.-L.; Zhang, Z.-X.; Sun, X.-Q.; Chang, T.; Guo, J.-F.; Huang, K.-K.; Zeng, H.-B.; Wang, D.-Y.; Yang, W.-S.; Zeng, R.-S.; Li, X.-M.; Xie, R.-G. Doped Emitting Cesium Silver Halides as X-Ray Scintillator with Fast Response Time, High Absorption Coefficient, and Light Yield. *Adv Photonics Res* **2021**, *2* (9), 2100066. https://doi.org/10.1002/ADPR.202100066.

(14) Yang, P.; Liu, G.; Liu, B.; Liu, X.; Lou, Y.; Chen, J.; Zhao, Y. All-Inorganic Cs2CuX4 (X = Cl, Br, and Br/I) Perovskite Quantum Dots with Blue-Green Luminescence. *Chemical Communications* **2018**, *54* (82), 11638–11641. https://doi.org/10.1039/C8CC07118G.

(15) Roccanova, R.; Yangui, A.; Seo, G.; Creason, T. D.; Wu, Y.; Kim, D. Y.; Du, M. H.; Saparov, B. Bright Luminescence from Nontoxic CsCu2X3(X = Cl, Br, I). *ACS Mater Lett* **2019**, *1* (4), 459–465. https://doi.org/10.1021/ACSMATERIALSLETT.9B00274/ASSET/IMAGES/MEDIUM/TZ9B00274_M004.GIF.

(16) Liu, S.; Yue, Y.; Zhang, X.; Wang, C.; Yang, G.; Zhu, D. A Controllable and Reversible Phase Transformation between All-Inorganic Perovskites for White Light Emitting Diodes. *J Mater Chem C Mater* **2020**, *8* (25), 8374–8379. https://doi.org/10.1039/D0TC01519A.

(17) Gu, Y.; Yao, X.; Long, M.; Geng, H.; Hu, M. Ultra-Broadband Light-Emitting Diodes from Co-Evaporated Lead-Free CsCu2I3. *Mater Lett* **2022**, *323*, 132607. https://doi.org/10.1016/J.MATLET.2022.132607.

(18) Xu, R.; Zhang, D.; Si, J.; Du, Y.; Hu, Q.; Hao, X.; Zhao, H.; Cai, P.; Ai, Q.; Yao, X.; Gao, Y.; Zhu, M.; Zhang, Z.; Cai, M.; Mo, H. W.; Harada, K.; Ye, Z.; Dai, X.; Adachi, C.; Liu, Z. Low-Voltage Driving Copper Iodide-Based Broadband Electroluminescence. *ACS Energy Lett* **2022**, *7* (12), 4408–4416.

https://doi.org/10.1021/ACSENERGYLETT.2C02471/ASSET/IMAGES/LARGE/NZ2C02471_0005.JPEG.

(19) Liu, W.; Zhu, K.; Teat, S. J.; Dey, G.; Shen, Z.; Wang, L.; O'carroll, D. M.; Li, J. All-in-One: Achieving Robust, Strongly Luminescent and Highly Dispersible Hybrid Materials by Combining Ionic and Coordinate Bonds in Molecular Crystals. *J. Am. Chem. Soc* **2017**, *139*. https://doi.org/10.1021/jacs.7b04550.

(20) Roccanova, R.; Yangui, A.; Seo, G.; Creason, T. D.; Wu, Y.; Kim, D. Y.; Du, M. H.; Saparov, B. Bright Luminescence from Nontoxic CsCu2X3(X = Cl, Br, I). *ACS Mater Lett* **2019**, *1* (4), 459–465. https://doi.org/10.1021/ACSMATERIALSLETT.9B00274/ASSET/IMAGES/MEDIUM/TZ9B00274_M004.GIF.

(21) Roccanova, R.; Yangui, A.; Seo, G.; Creason, T. D.; Wu, Y.; Do, ǁ; Kim, Y.; Du, M.-H.; Saparov, B. Bright Luminescence from Nontoxic CsCu 2 X 3 (X = Cl, Br, I). **2019**. https://doi.org/10.1021/acsmaterialslett.9b00274.

(22) Ma, Z.; Shi, Z.; Qin, C. C.; Cui, M.; Yang, D.; Wang, X.; Wang, L.; Ji, X.; Chen, X.; Sun, J.; Wu, D.; Zhang, Y.; Li, X. J.; Zhang, L.; Shan, C. Stable Yellow Light-Emitting Devices Based on Ternary Copper Halides with Broadband Emissive Self-Trapped Excitons. *ACS Nano* **2020**, *14* (4), 4475–4486. https://doi.org/10.1021/ACSNANO.9B10148/ASSET/IMAGES/LARGE/NN9B10148_0006.JPEG.

(23) Yang, B.; Yin, L.; Niu, G.; Yuan, J.-H.; Xue, K.-H.; Tan, Z.; Miao, X.-S.; Niu, M.; Du, X.; Song, H.; Lifshitz, E.; Tang, J.; Yang, B.; Yin, L.; Niu, G.; Yuan, J.; Xue, K.; Tan, Z.; Miao, X.; Du, X.; Song, H.; Tang, J.; Niu, M.; Lifshitz, E. Lead-Free Halide Rb2CuBr3 as Sensitive X-Ray Scintillator. *Advanced Materials* **2019**, *31* (44), 1904711. https://doi.org/10.1002/ADMA.201904711.

(24) Wang, B.; Tang, Y.; Yang, X.; Cai, W.; Li, R.; Ma, W.; Zhao, S.; Chen, C.; Zang, Z. Stable Yellow Light Emission from Lead-Free Copper Halides Single Crystals for Visible Light Communication. *Nano Materials Science* **2022**. https://doi.org/10.1016/J.NANOMS.2022.03.003.

(25) Du, M.-H. Emission Trend of Multiple Self-Trapped Excitons in Luminescent 1D Copper Halides. **2023**, *14*, 9. https://doi.org/10.1021/acsenergylett.9b02688.

(26) Wang, L.; Shi, Z.; Ma, Z.; Yang, D.; Zhang, F.; Ji, X.; Wang, M.; Chen, X.; Na, G.; Chen, S.; Wu, D.; Zhang, Y.; Li, X.; Zhang, L.; Shan, C. Colloidal Synthesis of Ternary Copper Halide Nanocrystals for High-Efficiency Deep-Blue Light-Emitting Diodes with a Half-Lifetime above 100 h. *Nano Lett* **2020**, *20* (5), 3568–3576. https://doi.org/10.1021/ACS.NANOLETT.0C00513/ASSET/IMAGES/LARGE/NL0C00513_0005.JPEG.

(27) Sun, F.; Liu, T.; Ran, P.; Chen, X.; Jiang, T.; Shen, W.; Liu, X.; Yang, Y. Top-Emitting Microcavity Light-Emitting Diodes Based on All-Thermally Evaporated Lead-Free Copper Halide Self-Trapped-Exciton Emitters. *Journal of Physical Chemistry Letters* **2022**, *13* (15),

3431–3437. https://doi.org/10.1021/ACS.JPCLETT.2C00740/ASSET/IMAGES/LARGE/JZ2C00740_0005.JPEG.

(28) Vashishtha, P.; Nutan, G. V.; E. Griffith, B.; Fang, Y.; Giovanni, D.; Jagadeeswararao, M.; Sum, T. C.; Mathews, N.; Mhaisalkar, S. G.; Hanna, J. V.; White, T. Cesium Copper Iodide Tailored Nanoplates and Nanorods for Blue, Yellow, and White Emission. *Chemistry of Materials* **2019**. https://doi.org/10.1021/ACS.CHEMMATER.9B03250/ASSET/IMAGES/MEDIUM/CM9B03250_M001.GIF.

(29) Ma, Z.; Shi, Z.; Qin, C. C.; Cui, M.; Yang, D.; Wang, X.; Wang, L.; Ji, X.; Chen, X.; Sun, J.; Wu, D.; Zhang, Y.; Li, X. J.; Zhang, L.; Shan, C. Stable Yellow Light-Emitting Devices Based on Ternary Copper Halides with Broadband Emissive Self-Trapped Excitons. *ACS Nano* **2020**, *14* (4), 4475–4486. https://doi.org/10.1021/ACSNANO.9B10148/ASSET/IMAGES/LARGE/NN9B10148_0006.JPEG.

(30) Guo, Q.; Zhao, X.; Song, B.; Luo, J.; Tang, J. Light Emission of Self-Trapped Excitons in Inorganic Metal Halides for Optoelectronic Applications. *Advanced Materials* **2022**, *34* (52), 2201008. https://doi.org/10.1002/ADMA.202201008.

(31) Kumawat, N. K.; Liu, X. K.; Kabra, D.; Gao, F. Blue Perovskite Light-Emitting Diodes: Progress, Challenges and Future Directions. *Nanoscale* **2019**, *11* (5), 2109–2120. https://doi.org/10.1039/C8NR09885A.

(32) Li, Y.; Vashishtha, P.; Zhou, Z.; Li, Z.; Shivarudraiah, S. B.; Ma, C.; Liu, J.; Wong, K. S.; Su, H.; Halpert, J. E. Room Temperature Synthesis of Stable, Printable Cs 3 Cu 2 X 5 (X = I, Br/ I, Br, Br/Cl, Cl) Colloidal Nanocrystals with Near-Unity Quantum Yield Green Emitters (X = Cl). *Chem. Mater* **2020**, *32*, 15. https://doi.org/10.1021/acs.chemmater.0c00280.

(33) Liu, N.; Zhao, X.; Xia, M.; Niu, G.; Guo, Q.; Gao, L.; Tang, J.; Liu, N.; Zhao, X.; Xia, M. L.; Niu, G. D.; Guo, Q. X.; Gao, L.; Tang, J. Light-Emitting Diodes Based on All-Inorganic Copper Halide Perovskite with Self-Trapped Excitons. *J. Semicond 2020* (5), 52204. https://doi.org/10.1088/1674-4926/41/5/052204.

(34) Mandal, T. N.; Roy, S.; Barik, A. K.; Gupta, S.; Butcher, R. J.; Kar, S. K. Unusual Complexation of Cu(I) by Pyrimidine/Pyridine-Pyrazole Derived Ligands Exploiting the Molecular Function of 2-Mercapto-4,6-Dimethylpyrimidine – Syntheses, Crystal Structures and Electrochemistry. *Inorganica Chim Acta* **2009**, *362* (4), 1315–1322. https://doi.org/10.1016/J.ICA.2008.06.027.

(35) Rastrelli, F.; Bagno, A. Predicting the NMR Spectra of Paramagnetic Molecules by DFT: Application to Organic Free Radicals and Transition-Metal Complexes. *Chemistry – A European Journal* **2009**, *15* (32), 7990–8004. https://doi.org/10.1002/CHEM.200802443.

(36) Febrian, R.; Roddy, J. P.; Chang, C. H.; Devall, C. T.; Bracher, P. J. Removal of Paramagnetic Ions Prior to Analysis of Organic Reactions in Aqueous Solutions by NMR

Spectroscopy. *ACS Omega* **2021**, *6* (23), 14727–14733. https://doi.org/10.1021/ACSOMEGA.9B02610/ASSET/IMAGES/LARGE/AO9B02610_0005.JPEG.

(37) Khan, Q.; Subramanian, A.; Ahmed, I.; Khan, M.; Nathan, A.; Wang, G.; Wei, L.; Chen, J.; Zhang, Y.; Bao, Q. Overcoming the Electroluminescence Efficiency Limitations in Quantum-Dot Light-Emitting Diodes. *Adv Opt Mater* **2019**, *7* (20), 1900695. https://doi.org/10.1002/ADOM.201900695.

(38) Li, Z.; Chen, Z.; Yang, Y.; Xue, Q.; Yip, H. L.; Cao, Y. Modulation of Recombination Zone Position for Quasi-Two-Dimensional Blue Perovskite Light-Emitting Diodes with Efficiency Exceeding 5%. *Nat Commun* **2019**, *10* (1). https://doi.org/10.1038/S41467-019-09011-5.

(39) Wong, T. C.; Kovac, J.; Lee, C. S.; Hung, L. S.; Lee, S. T. Transient Electroluminescence Measurements on Electron-Mobility of N-Arylbenzimidazoles. *Chem Phys Lett* **2001**, *334* (1–3), 61–64. https://doi.org/10.1016/S0009-2614(00)01442-1.

(40) Chiu, C. H.; Amin, N. R. Al; Xie, J. X.; Lee, C. C.; Luo, D.; Biring, S.; Sutanto, K.; Liu, S. W.; Chen, C. H. A Phosphorescent OLED with an Efficiency Roll-off Lower than 1% at 10000 Cd m −2 Achieved by Reducing the Carrier Mobility of the Donors in an Exciplex Co-Host System. *J Mater Chem C Mater* **2022**, *10* (12), 4955–4964. https://doi.org/10.1039/D1TC04473G.

(41) Shi-Jian Su, B.; Chiba, T.; Takeda, T.; Kido, J.; Su, S.; Takeda, T.; Kido, J.; Chiba, T. Pyridine-Containing Triphenylbenzene Derivatives with High Electron Mobility for Highly Efficient Phosphorescent OLEDs. *Advanced Materials* **2008**, *20* (11), 2125–2130. https://doi.org/10.1002/ADMA.200701730.

(42) Chaney, R. C.; Lafon, E. E.; Lin, C. C. Energy Band Structure of Lithium Fluoride Crystals by the Method of Tight Binding. *Phys Rev B* **1971**, *4* (8), 2734. https://doi.org/10.1103/PhysRevB.4.2734.

(43) Liu, S. Y.; Chang, J. H.; Wu, I. W.; Wu, C. I. Alternating Current Driven Organic Light Emitting Diodes Using Lithium Fluoride Insulating Layers. *Scientific Reports 2014 4:1* **2014**, *4* (1), 1–7. https://doi.org/10.1038/srep07559.

(44) Gangishetty, M. K.; Hou, S.; Quan, Q.; Congreve, D. N.; Gangishetty, M. K.; Hou, S.; Quan, Q.; Congreve, D. N. Reducing Architecture Limitations for Efficient Blue Perovskite Light-Emitting Diodes. *Advanced Materials* **2018**, *30* (20), 1706226. https://doi.org/10.1002/ADMA.201706226.

(45) Forrest, S. R.; Bradley, D. D. C.; Thompson, M. E. Measuring the Efficiency of Organic Light-Emitting Devices. *Advanced Materials* **2003**, *15* (13), 1043–1048. https://doi.org/10.1002/ADMA.200302151.